Carbon Trends 7 (2022) 100156

Contents lists available at ScienceDirect

Carbon Trends

journal homepage: www.elsevier.com/locate/cartre

Characterization and electrical analysis of carbon-based solid lubricant coatings

Bruno Alderete[a], Frank Mücklich[a], Sebastian Suarez[a,*]

[a] Chair of Functional Materials, Saarland University, Campus D3.3, 66123 Saarbrücken Germany

ARTICLE INFO

Article history:
Received 3 November 2021
Revised 18 January 2022
Accepted 18 January 2022

Keywords:
Carbon nanohorns
Carbon nanotubes
Electrical connector lubrication
Electrical contact resistance
Electrophoretic deposition
Graphene oxide
Graphite flakes

ABSTRACT

The use of electrical devices has skyrocketed over the past decades, increasing the demand for electrical connectors worldwide. Therefore, it is of utmost importance to produce more reliable, energy and material efficient, and durable electrical contact material systems; particularly in low-redundancy systems, such as in passenger vehicles. This work analyzes the potential use of carbon nanoparticle coatings applied via electrophoretic deposition over copper substrates to reduce wear, require lower insertion forces, and to protect the connectors from atmospheric conditions, while reducing the gain on the overall resistance of the system. Four carbon nanoparticles were considered due to their well-known solid-lubricating capabilities, namely: graphite flakes, graphene oxide, carbon nanotubes, and carbon nanohorns. Through a comprehensive characterization of the coatings, aspects like coating topography, compactness, thickness, elasticity, and electrical contact resistance were analyzed. Carbon nanotubes and nanohorns proved to have the highest potential. In addition to their previously documented outstanding solid-lubricity and environmental protection - after chemical modification of the coatings' surfaces - these nanoparticles showed low resistance values for loads above 4 N, i.e., below 400 mΩ. Moreover, the coatings produced were thin and homogeneous, with adequate mechanical stability, and elastic behavior.

1. Introduction

Over the past decades the use of electrical connectors has significantly increased. These components are ubiquitously found throughout a wide range of devices used in day-to-day life. Their use ranges from ordinary tasks (such as vacuum cleaning, water heating, etc.) up to applications where their correct performance is crucial for the safety of the users (e.g., navigation in passenger aircrafts, industrial machinery, among others). The rising trend in the consumption of electronic and smart devices - as well as the growing digitization of industrial processes - has spiked the demand for electrical components. Experts predict that the connector industry will register a 7% increase in compound annual growth rate between the years 2020 and 2026 (according to Global Market Insights Inc.), surpassing a total revenue of 61 billion Euro. This trend is not new, in the year 2000 alone connector sales were approximately 30 billion Euro [1]. Half of those sales were destined for the computer and telecommunication market, whereas 5 billion Euro in sales corresponded to the automotive industry. This scenario clearly highlights the importance of efficient, durable, and more reliable electrical connectors. The reliability of an electrical connector takes a more important role in low redundancy systems, such as in passenger vehicles. Here, most electrical circuits rely on only one connector to effectively open and close the circuit. Therefore, one electrical connector failing can potentially affect the entire system.

There are several atmospheric and tribological conditions that considerably reduce the duty life of electrical connectors. Regarding ambient conditions, contact materials react with agents present in the atmosphere, such as oxygen, sulfur, corrosive agents, acids, etc., depending on the application. Moreover, electrical connectors are subjected to wear during mating and un-mating cycles and fretting wear during normal operations. To reduce wear on the electrical connectors lubricant greases are applied on their surface. Greases are used since they do not easily wash off, therefore reducing the requirement of reapplication [2]. Using lubricant greases help prevent undesired reactions with atmospheric conditions, along with reducing wear, fretting, and the insertion force required. The greases also prevent the access of water in the contact. Connector lubricants consists of varying chemistry; they can

* Corresponding author at: Functional Materials, Dept. of Materials Science and Engineering, Functional Materials Institute - Saarland University, Campus D3.3, room 2.11, D66123 Saarbruecken, Germany.
E-mail address: s.suarez@mx.uni-saarland.de (S. Suarez).

https://doi.org/10.1016/j.cartre.2022.100156

be mineral or synthetic based oils with thickeners (e.g., polyurea-based thickeners). However, these lubricants increase the electrical resistance, therefore hindering their conductive properties. So far, this has been a favorable trade off since the greases extended their duty life.

Copper is among the most used metals for electrical connectors. It has the second lowest resistivity among metallic conductors (1.65 x 10^{-8} Ω.m at 20 °C) [2], being silver the best metallic conductor. Copper has adequate mechanical properties, and its surface is protected from oxidation as a consequence of a native oxide layer that is spontaneously formed on its surface. Although copper oxide is detrimental to its conductive properties, it effectively protects the metal from further degradation. Copper electrical connectors are generally plated with soft metals, such as gold, silver, or tin.

Carbon is a versatile element capable of forming different carbon-carbon bonds. Depending on the hybridization state, different allotropes are formed with varying properties [3,4]. In this work we explore alternative solutions to lubricating contacts so as to not compromise the electrical characteristics of the interfaces. Therefore, we propose carbon nanoparticle (CNP) coatings obtained via electrophoretic deposition on copper substrates. The CNP selected are graphite flakes (GF), graphene oxide (GO), carbon nanotubes (CNT), and carbon nanohorns (CNH). These CNP were chosen based on their well reported lubricant properties [5,6,7], with the added advantage of their exceptional transport properties due to the delocalized p_z orbital, characteristic of sp^2 carbon.

Graphite is a classical, well-known solid lubricant due to the weak interlayer interactions of the stacked hexagonal carbon structures. Therefore, graphite shows low shear strength when subjected to friction, describing its use as solid-state lubricant and its self-lubricating properties [8,9,10,11,12,13]. Due to its intrinsic lubricity, graphite has also been introduced as an additive in oils, commonly referred to as “nanofluids” [14,15]. Graphite additionally presents good transport properties, namely thermal and electrical conductivity. However, due to the stacking of the hexagonal layers it presents anisotropy. In-plane, the thermal and electrical conductivity are significantly lower than perpendicularly, relative to the surface of the individual graphite layers. Nonetheless, studies have shown that graphite presents 2000 to 4000 $W.m^{-1}.K^{-1}$ for large sized perfect structures, and electrical conductivity between 400 and 1250 $S.cm^{-1}$ [16,17,18]. Consequently, this allotrope was selected for two key reasons. Foremost, it is considered a benchmark since it is widely used as a solid lubricant. And more importantly, it presents good electrical properties. Furthermore, since graphite is a hydrophobic material, graphite coatings have promising applications as surface protection barriers [19].

Graphene oxide is a slightly lower quality material, with reduced physical properties compared to graphene [18,20–28]. GO can be obtained from graphite by chemical exfoliation (top-down method) [29]. Alternatively, GO can be obtained from graphite by Hummer’s method or Brodie’s method [30,31]. By undergoing an additional reduction step, reduced graphene oxide (rGO) can be obtained. This rGO still possesses some imperfections, but it is relatively similar to graphene regarding its physical properties. GO is not as conductive as rGO or graphene (the electrical conductivity of rGO is linked to the reduction agent and reduction times) as a consequence of the carbon-oxygen bonds [32]. Furthermore, the covalent bonds between oxygen and the functional groups in GO generate structural defects in the crystalline structure. These defects scatter the electrons, affecting GO’s electrical conductivity [23]. However, it is simpler to mass produce at a lower cost. GO is particularly interesting as a solid lubricant due to the oxygen bonds present in the lattice. As the oxygen bonds repel one another, they prevent the graphene sheets from re-stacking and thus forming graphite. This further decreases the shear forces during friction. Consequently, GO has been of great interest for applications as solid lubricant, self-lubricating solid, and as a lubricant additive [33,34,35]. Moreover, due to the oxygen present in GO, atmospheric protection may be affected due to an increased hydrophilic behavior. Nonetheless, studies have shown that the wetting behavior of GO can be altered by chemical modifications [36,37].

Carbon nanotubes have been of great interest to the research community in the past decades due to their outstanding intrinsic physical properties and their potential fields of application. These quasi-one-dimensional carbon structures - in their purest defect-free state - have the highest tensile strength of any material known, the highest thermal conductivity, and quasi-ballistic electronic conduction. The theoretical thermal conductivity of CNT was reported to be over 6000 $W.m^{-1}.K^{-1}$, whereas the electrical conductivity varies between 10^2 to 10^5 $S.cm^{-1}$ [38–46]. However, due to their geometry, CNT present anisotropy in their transport properties, showing better thermal and electrical conductivity in the axial direction compared to radial direction. Moreover, the excelling intrinsic properties of CNT are hindered by their tendency to form agglomerates (due to π-π interactions) [47,48]. Therefore, breaking up the CNT agglomerates without causing damage to the structure of the individual CNT is of utmost importance in order to maintain their properties. Previous reports have shown that CNT have promising applications as protective barriers from atmospheric conditions [49], as well as self-lubricating metal matrix composites and coatings [50–52]. Similarly to graphite, CNT have been used as additives to improve the lubricity of traditional oil-based lubricants [53–55]. In this work multi-walled CNT are used due to their simpler synthesis method, lower cost, and - most importantly - since statistically multi-walled CNT always have at least one conductive wall.

Single walled carbon nanohorns - also known as nanocones - are part of the sp^2 carbon family which have not received as much attention as the previously discussed CNP. CNH are nanoparticles with a tubular shape, similar to single-walled CNT [56–59]. However, CNH arrange themselves in horn-like endings, with tube diameters in the range of 2 to 5 nm and tube lengths between 40 and 50 nm. CNH present two important advantages over CNT, namely: 1) CNH synthesis does not require metallic catalyst, and 2) CNH can be produced on a large scale at room temperature. CNH are also differentiated from CNT because all CNH are semiconducting. Their conductive properties are closely linked to temperature and the adsorption of gases. As for all semiconductors, CNH show higher electrical conductivity at higher temperatures. Due to CNH morphology, they are of interest in solid lubrication applications and as oil-based lubricant additives [60]. Regarding the electron transport properties of CNH, a specific value was not found. However, one study has shown that incorporating CNH in organic aerogel composites has increased its electrical conductivity [61]. Moreover, it has been previously shown that CNH have a hydrophobic behavior [62]. Consequently, CNH coatings could potentially be used as protective barriers by manipulating their superficial characteristics, as previously shown for CNT.

Electrophoretic deposition (EPD) is a relatively straight forward method used to deposit CNP [49,63–70]. This method was selected due to its simplicity, easily controllable coating thicknesses, modest equipment requirements, and up-scalability. In essence, this technique requires the previous dispersion of the CNP in a suitable solvent. The electrodes are later immersed in the colloidal suspension and connected to a direct current power source. An electric field is generated, imparting electrophoresis on the CNP. The stability of the dispersion depends on the size of the CNP agglomerates. Therefore, mechanically breaking down the agglomerate size is crucial. Agglomerate size can be reduced through homogenization (shear force) and through sonication (ultrasound bath) [49,70]. Smaller particle sizes also promote more homogeneous coatings

and require weaker electric fields. The stability of the colloid is further improved by adding an additive to the solution. It has already been proven that triethylamine (henceforth TEA) improves the overall stability of the colloid, and assists the deposition process by giving the CNP a positive superficial charge (anodic deposition) [49,71].

A study carried out by Lloyd et al. has laid the foundation for graphite, graphene and CNT as electrical connector finishing layer [72]. Their study focused on the tribological and electrical behavior of thin coatings deposited by spray coating (and/or brushed) on Au, Ag and Sn surfaces. However, the normal loads applied for resistance measurements were low, 0.5 N for Au and 2 N for Ag and Sn. Within the scope of this work, we comprehensively analyze the potential use of four different CNP-based coatings obtained via EPD to increase the efficiency of electrical connectors. Additionally, these CNP have superior thermal conductivity, enhancing the dissipation of the heat that is produced in the electrical contact. Furthermore, depending on the resulting chemistry of the coating's surface, these can behave as near superhydrophobic surfaces [49]. The resulting coatings should lubricate the connector for mating and un-mating, protect the connector from ambient conditions, while minimizing the effect on the electrical conductivity of the system.

The coating's morphology was evaluated using scanning electron microscopy/focused ion beam (SEM/FIM) and confocal laser scanning microscopy (CLSM). From these techniques crucial information on the coating's topography, thickness, homogeneity, compactness, and interface was acquired. Additionally, the deposition rate of the CNP was qualitatively analyzed with the information acquired from FIB cross sections. SEM on the pristine nanoparticles was carried out, measuring their minimum, maximum, and mean particle/agglomerate size. Load-dependent electrical contact resistance (ECR), using a self-developed setup, was used to characterize the electrical properties of the coatings. Moreover, post-ECR CLSM measurements were carried out on the coated samples and the counter electrode. The two latter were the primary focus of this study since the electrical resistance and durability of the coatings plays a pivotal role in the efficiency and reliability of the connector.

2. Materials and method

The substrates used were laminated, flat pure-copper platelets (25 × 10 × 1) mm. These Cu platelets were ground (P1200 grit silicon carbide grinding paper) and polished at 6 µm, 3 µm, and 1 µm to obtain a mirror-polished surface before coating. Graphite flakes (Alfa Aesar, Germany) with a median size between 7 and 10 µm, 99.8% purity were used. The graphene oxide particles possess 51.25 wt% carbon, 43.99 wt% oxygen (Nanoinnova Technologies, Spain). The CNT used were chemical vapor deposition-grown multiwalled CNT (Graphene Supermarket, USA), with an outer diameter distribution between 50 and 85 nm, an as-received state length from 10 to 15 µm, and carbon purity over 94%. The single-walled CNH used were dahlia-type, produced by rapid condensation of carbon atoms without a catalyst by Carbonium SRL, Italy. The as-received high-purity CNH have a horn diameter between 3 and 5 nm, horn length between 30 and 50 nm, and a cluster diameter between 60 and 120 nm.

A schematic representation of the EPD setup is shown in **Fig. 1**. Due to the geometry of the electrodes (flat, rectangular platelets), the electric field is perpendicular to the parallel-mounted electrodes. A copper sample was used as a counter electrode. The power source used (Consort EV3020) operates under constant voltage (potentiostatic EPD). Therefore, to alter the strength of the electric field, the voltage must be manipulated. From previous studies [58], it was found that the optimal voltage level for EPD of CNP is 300 V. Due to the geometric constraints of the setup, the

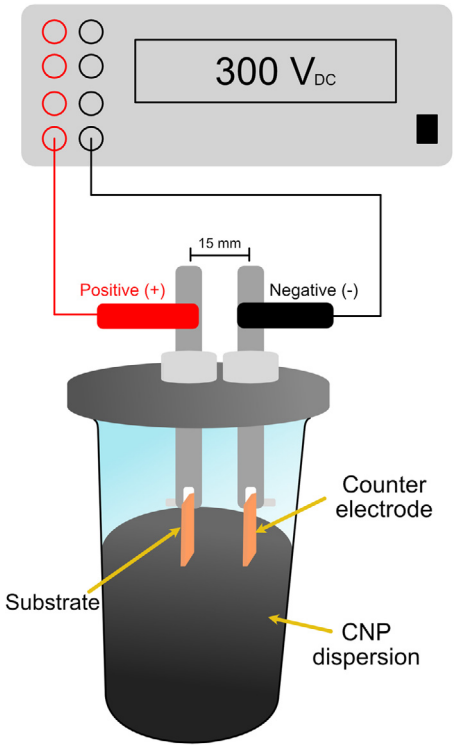

Fig. 1. Schematic representation of EPD setup.

minimum inter-electrode distance was 15 mm. Reducing the inter-electrode distance minimizes the distance the CNP must travel to reach the deposition electrode. Keeping this voltage and inter-electrode distance constant, the coating thickness is controlled by the duration of the deposition process. The deposition rate varies from nanoparticle to nanoparticle, depending on their conductivity. It is important that each CNP has enough time to fully coat the substrate during EPD. Therefore, the coatings obtained will be compact and without voids. This is highly desirable since uncoated regions lack wear and atmospheric protection. Furthermore, regarding ECR measurements, these regions will behave significantly different than completely coated regions.

The dispersion of the carbon nanoparticles consists of mixing them in a solvent, Isopropanol (IPA), and an additive. As previously mentioned, the role of the additive is to enhance the stability of the dispersion and provide a superficial charge to the nanoparticles. According to the additive used, the superficial charge of the nanoparticles varies, consequently changing the deposition electrode. In this study, TEA ($C_6H_{15}N$) was the additive used. The homogenization step begins once the solvent, additive, and nanoparticles have been added into a beaker. The homogenizer (IKA T25 digital Ultra-Turrax) breaks down the nanoparticle agglomerates using shear forces. To further separate the nanoparticles, the colloid is placed in an ultrasonic bath (Bandelin Sonorex Super RK 514 BH, 33 Hz, 860 W). The concentrations used and the dispersion times are described in detail in **Table 1**.

As previously mentioned, the deposition rate varies depending on the conductivity of each CNP. A common deposition time of 5 minutes was chosen for all CNP to achieve a uniform, homogeneous, and thin coating. Thick coatings would result in an additional barrier for electrical current. Therefore, thinner coatings are sought out, hence the benefits attained would outweigh the gain in ECR caused by the CNP coating. The produced coatings were characterized with SEM/FIB (FEI Helios NanoLab600 Dual Beam Setup) and Confocal Laser Scanning Microscopy (LEXT OLS4100, Olympus). The SEM micrographs were acquired using an acceleration voltage

Table 1
. Concentrations and dispersion times for each CNP colloid.

Nanoparticle	GF	GO	CNT	CNH
Nanoparticle concentration / mg/ml	0.2	0.5	0.2	0.05
IPA / ml	80			70
TEA / ml	10	10	5	5
Homogenizer / min	10	5	5	10
Homogenizer speed / rpm	7000			12000
Ultrasound / min	10			15

Table 2
. Mean particle/agglomerate size of pristine CNP.

Nanoparticle	GF	GO	CNT	CNH
Mean particle size	(7.1 ± 2.2) µm			(74 ± 18) nm
Agglomerate size		(5.0 ± 1.9) µm	(6.6 ± 4.2) µm	(264 ± 70) nm
Min. size	4.1 µm	2.2 µm	2.1 µm	Particle: 13 nm Agglomerate: 154 nm
Max. size	12.4 µm	7.8 µm	19.5 µm	Particle: 29 nm Agglomerate: 388 nm

of 5 kV and an electron beam current of 1.4 nA. The intensity maps and height profiles acquired with the CLSM were taken with 50× magnification and a laser wavelength of 405 nm. The profiles consist of a 3×3 stitching of the region of interest.

The four coatings and the substrate were electrically characterized via a self-developed ECR testing rig [73–75]. This rig can analyze load dependent ECR of the material via four-terminal method using a direct-current power source. Loading and unloading cycles from 0.25 up to 10 N can be measured. The power source used was a Keithley 2400 SMU, capable of sourcing between 1 nA and 1.05 A. This device can also source voltage, but for this method constant current was sourced, and the voltage drop between electrodes registered. The current was set at 100 mA to stay in the dry circuit conditions [76,77]. The voltage drop is measured using a Keithley 2182a nanovoltmeter. This device can be set at five different measurement ranges, i.e., 10 mV, 100 mV, 1 V, 10 V, and 100 V. Depending on the voltage range that is expected for the measurement, the instrument range must be selected accordingly. It is noteworthy that the lowest suitable range for the measurement must be chosen to minimize the uncertainty of the measurement [78].

One ECR measurement cycle was measured for each coating and the substrate. Each cycle consisted of one loading and one unloading semi-cycle. Ten ECR measurements are taken per load throughout the cycle. Depending on the voltage drop recorded, the range of the nanovoltmeter must be adjusted to prevent the device from overflowing. If the range is too low, the recorded value will be incorrect; whereas in selecting a range that is too high the uncertainty of the measurement increases [78]. The normal loads that constitute the cycles are: 0.5 N, 1 N, 2 N, 3 N, 4 N, 5 N, 6 N, 8 N, and 10 N. Two-cycle ECR measurements were taken using the same loads and current. This allowed an analysis on the deformation of the coatings.

In this setup, the coated sample was the electrode and a silver-nickel core ($AgNi_{0.15}$), hard gold coated rivet ($AuCo_{0.2}$) was used as counter electrode (Adam Bornbaum GmbH). The counter electrode had a curved head, with a mean curvature of 4 mm at its tip. The roughness of the rivet's tip was analyzed with CLSM with a laser wavelength of 405 nm and 20× objective. The root mean square roughness was S_q = 0.255 µm. For each coated sample, a new rivet was used. The same rivet was used for all subsequent measurements carried out on the same coating.

The pristine CNP were observed with SEM. Quantification on pristine CNP powders were carried out with ImageJ software on micrographs with a magnification of 2500×, except for the CNH where 50000× was used. The minimum, maximum and average particle/agglomerate sizes are summarized in **Table 2**. As this table shows, the mean GF particles size falls within the range provided by the manufacturer (7-10 µm). However, larger flakes up to 12.4 µm where observed. The GF observed were randomly distributed, without a specific orientation, showing multiple folded particles. On top of the larger GF particles, smaller GF were observed. GO showed large networks of agglomerated particles. A few significantly larger GO particles could be identified. The agglomerated GO particles interact with one another, making it difficult to differentiate one agglomerate from another. CNT showed varied agglomerate sizes. Agglomerates of 2.1 µm up to 19.5 µm were observed, with a mean size of 6.6 µm. The diameter of the CNT was also measured on a micrograph with 50000×. The mean CNT diameter measured was 45 nm with a standard deviation of 12 nm, in accordance with the values provided by the manufacturer. The CNH particles and clusters could both be measured. The mean CNH particle diameter measured was approximately 74 nm, whereas the mean cluster size was approximately 265 nm. CNH agglomerate sizes range from 154 nm up to 388 nm approximately. Regarding CNH particles, the smallest particle observed was 13 nm in diameter approximately, whereas the maximum particle diameter was 29 nm.

3. Results and discussion

3.1. Coating topographic characterization

SEM micrographs of the four coatings are shown in **Fig. 2**. From these micrographs one can obtain information on the different topographies obtained from each CNP coating. As **Fig. 2a** shows, GF are deposited with different orientations, with clusters of horizontally deposited GF and few vertically deposited GF. This leads to an uneven coating, with visible voids (some of which are highlighted in light green). This could potentially lead to a porous coating. The inset micrograph on the top right corner shows the pristine GF particles. As the inset illustrates, GF particles significantly vary in size and shape. It is interesting to highlight that GF do not form agglomerates. GO coating's topography is shown in **Fig. 2b**. This coating is similar to the GF coating, with an uneven surface and multiple voids (highlighted in light green). GO agglomerates can be seen throughout the surface, as well as large GO particles (shown by the yellow arrows). The particles deposited horizontally on the surface of the substrate will present a higher resistance, whereas the vertically deposited particles will conduct electrical current with lower resistance since in-plane conductivity is significantly higher. The top right inset shows a micrograph of pristine GO nanoparticles. In contrast to what was observed in graphite, GO does forms agglomerates. Bundles of GO particles are ubiquitous throughout the

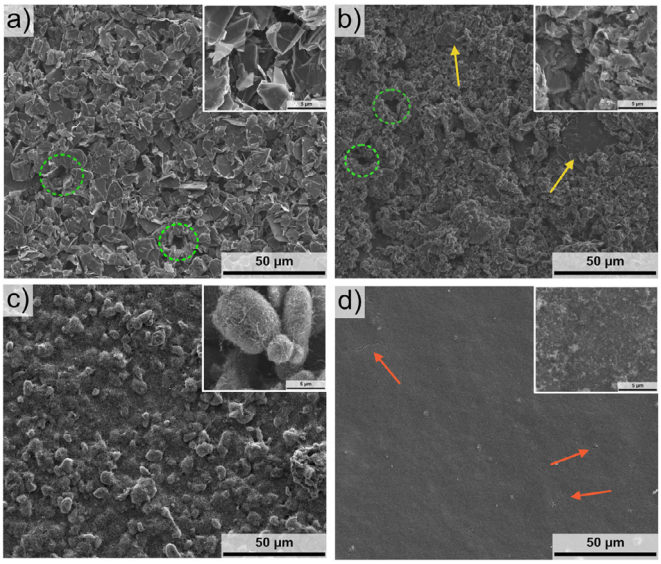

Fig. 2. Secondary electron micrographs of coating topography – a) GF, b) GO, c) CNT, and d) CNH. Light green circles highlight the presence of voids on the coatings' surface. The yellow arrows indicate the inclusion of larger GO particles. The red arrows indicate the presence of fissures on the CNH coating's surface. A micrograph of each pristine CNP is shown as an inset in the top right corner.

micrograph, making it difficult to identify individual GO particles. Nonetheless, individual larger GO particles can be distinguished among the GO bundles (lower left of the inset). The CNT coating, shown in **Fig. 2c**, presents a heterogeneous surface, with large CNT agglomerates scattered throughout its surface. Thicker regions can be seen where the agglomerates are present. The thinner regions correspond to small CNT agglomerates. However, the substrate cannot be seen suggesting that the entirety of the surface is coated. This is an advantage regarding wear and atmospheric protection, and consistency in contacting surfaces. Nonetheless, regions with larger CNT agglomerates could produce an increase in the electrical resistance. The inset at the top right shows a few pristine CNT agglomerates at higher magnification. In this inset the varying size of the agglomerates can be highlighted. Furthermore, the inset shows how the agglomerates tend to bundle, increasing the overall agglomerate size. Finally, **Fig. 2d** shows the SEM micrograph of the CNH coating. This figure shows a uniform surface with no topography. It does, however, present some small cracks (shown by the red arrows). These cracks may be a consequence of the elevated voltage used in EPD, and the drying of the coating after removal from the colloid [58]. These cracked surfaces jeopardize the transport properties and atmospheric protection characteristics of the coating. The inset in the top right shows the pristine CNH nanoparticles. Due to the dimensions of the CNH only larger agglomerates can be observed at this magnification. They are identifiable by the lighter shade in the SEM micrograph.

Observing the four surfaces, the CNH coating seems to be the most homogeneous and compact coating. Contrarily, the GF and GO coatings appear to be highly porous and heterogeneous. In the case of GF, the uneven coating can be explained by the large size of the particles. Relative to the GF coating, GO appears to be - to a moderate extent - more homogeneous. Although, several voids can be observed on its surface. Concerning the CNT coating, it is considered a heterogeneous coating. However, compared to GF and GO coatings, it appears to be a better alternative as voids cannot be observed. Nonetheless, the thickness of the coating changes significantly from region to region as a consequence of the larger agglomerates.

For further characterization of the coatings' topography, secondary electron images were acquired with the samples tilted to 52° relative to the electron beam. Their surfaces were additionally analyzed with CLSM, plotting their height profile. The height profile and SEM micrograph are shown in **Fig. 3**. The micrograph and height profile correspond to different regions in the coatings. The height profile and micrograph in **Fig. 3a** and **Fig. 3b**, respectively, correspond to the GF coating. These figures prove what the micrograph from **Fig. 2a** suggested; the coating produced by GF is highly irregular. The height profile of the GF coating shows that, on average, the height of the coating is in the range of 20 µm. This plot also shows that the coating has multiple voids and peaks scattered throughout the analyzed region. This can be seen by the distribution of blue and yellow/orange regions in the height profile. The peaks and valleys of the coating are also depicted in the tilted SEM micrograph. The valleys are found at an approximate height of 7 µm and the peaks at about 28 µm. **Fig. 3c** and **Fig. 3d** show the height profile and micrograph of the GO coating, respectively. Both figures show the irregularities and uneven nature of the coating. The irregularities are accentuated when compared to the GF coating. Although the SEM micrograph shows that the GO coating has many voids, it can be seen from the height profile that the voids are superficial. In other words, the voids are close to the surface of the coating. Furthermore, this coating has regions where the GO particles have been deposited higher than in other regions, as seen in the height profile (orange/red regions). The mean height of the coating is in the 20 µm range, with peaks as high as 35 µm and valleys around 10 µm. Observing the tilted micrograph, it can be seen that the higher regions in the coating correspond to GO agglomerates, but also due to large GO particles. These particles are significantly larger than the GO agglomerates, with sizes comparable to those of the GF particles. The height profile and micrograph of the CNT coating is shown in **Fig. 3e** and **Fig. 3f**, respectively. This coating highly contrasts with the previous two. The height profile shows that the mean height is approximately 10 µm with high peaks corresponding to the agglomerates (approximately 20 µm high). Both the height profile and the micrograph show that the coating does not present voids. The height difference on the coating's surface is solely a consequence of the large CNT agglomerates. These agglomerates produce the heterogeneity of the coating. Finally, **Fig. 3g** and **Fig. 3h** shows the height profile and micrograph of the CNH coating, respectively. These figures confirm that this coating is highly homogeneous, as suggested by the SEM micrograph from **Fig. 2d**. The average height of this coating is below 10 µm, with a few peaks reaching an approximate height of 14 µm. These peaks are seen as spots on the micrograph. These spots are a consequence of relatively large CNH agglomerates. The fissures observed on the SEM micrographs are not detected in the height profile. Therefore, the depth of the fissures can be neglected.

The height profiles acquired with CLSM provide additional information, complementing the information obtained from SEM microscopy. From **Fig. 3** we can establish that GF and GO produce irregular surfaces, being the former more heterogeneous than the latter. This statement contradicts what was initially hypothesized by observing the SEM micrographs in **Fig. 2**. The CNH coating is exceptionally homogeneous, with very few outlaying CNH agglomerates. The CNT coating stands in the middle showing heterogeneity, but to a lesser extent than GF and GO coatings. The tilted micrograph additionally allows the visualization of superficial voids. These are ubiquitously found in the GF and GO coatings, being more prominent in the former as demonstrated by the height profile.

3.2. Coating cross section

For an in-depth assessment of the compactness, thickness and coating-substrate interface, FIB cross sections on each of the coatings were carried out, shown in **Fig. 4**. In all cases, the substrate-

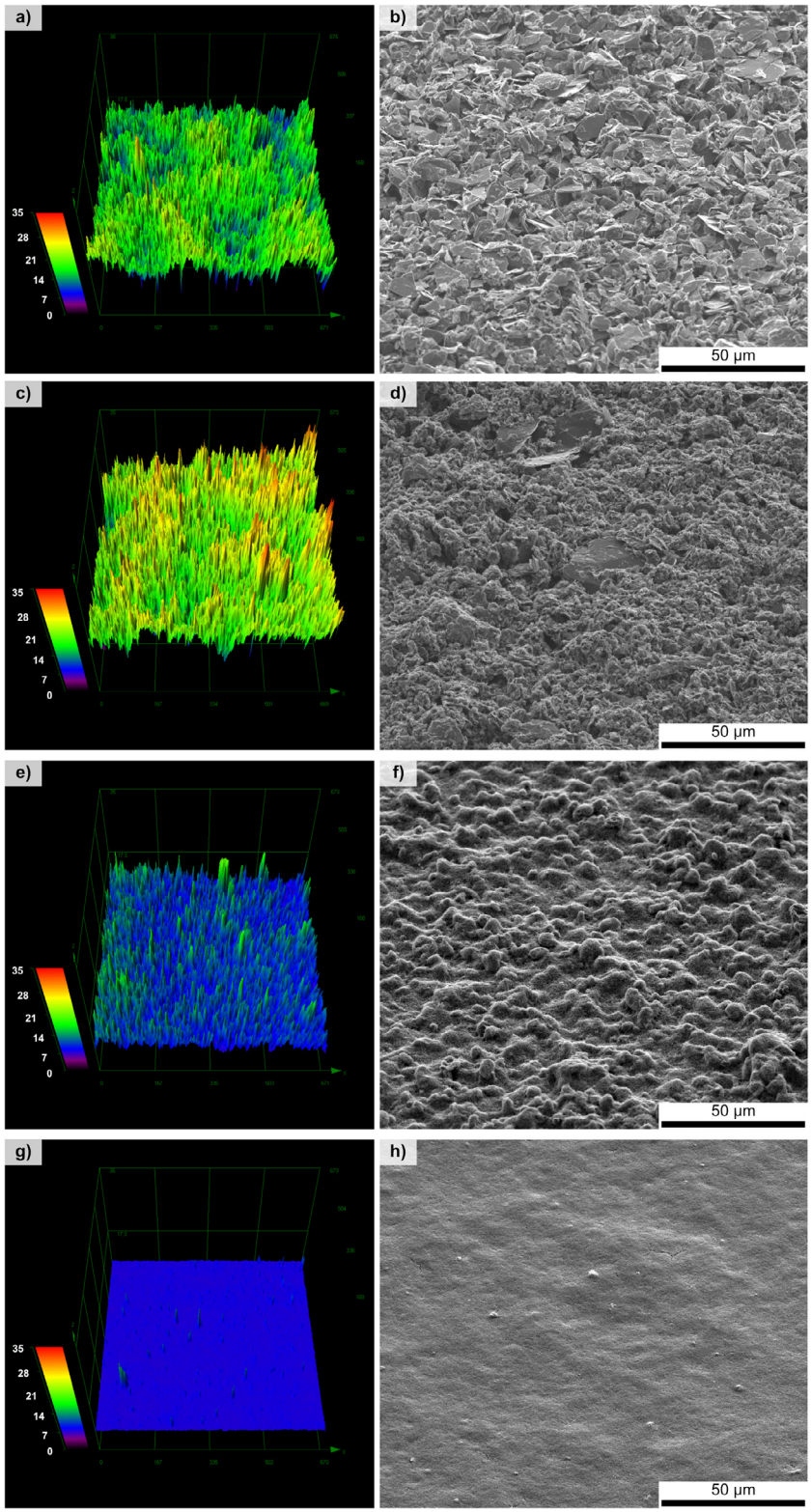

Fig. 3. CLSM height profile (left), secondary electron micrograph of coatings tilted at 52° relative to electron beam (right); a-b) GF, c-d) GO, e-f) CNT, and g-h) CNH. It is important to highlight that the height profile and SEM micrograph do not correspond to the same region of the coatings. The tilted SEM micrographs were taken on the same regions as the micrographs shown in Fig. 2.

coating interface is highlighted by a green line. Likewise, the surface of the coating is shown with a green dashed line.

The GF coating is shown in **Fig. 4a**. From the SEM image in **Fig. 2a**, the coating seemed highly heterogeneous. However, the cross section shows that the thickness of the coating does not vary significantly. This coating has an average thickness of 12.8 ± 0.9 µm. The uniformity of the coating is evidenced by the marginal standard deviation, accounting for only 7% variation in the overall thickness of the coating. This is in strong contrast from what one can infer from the SEM micrographs. The coating is relatively

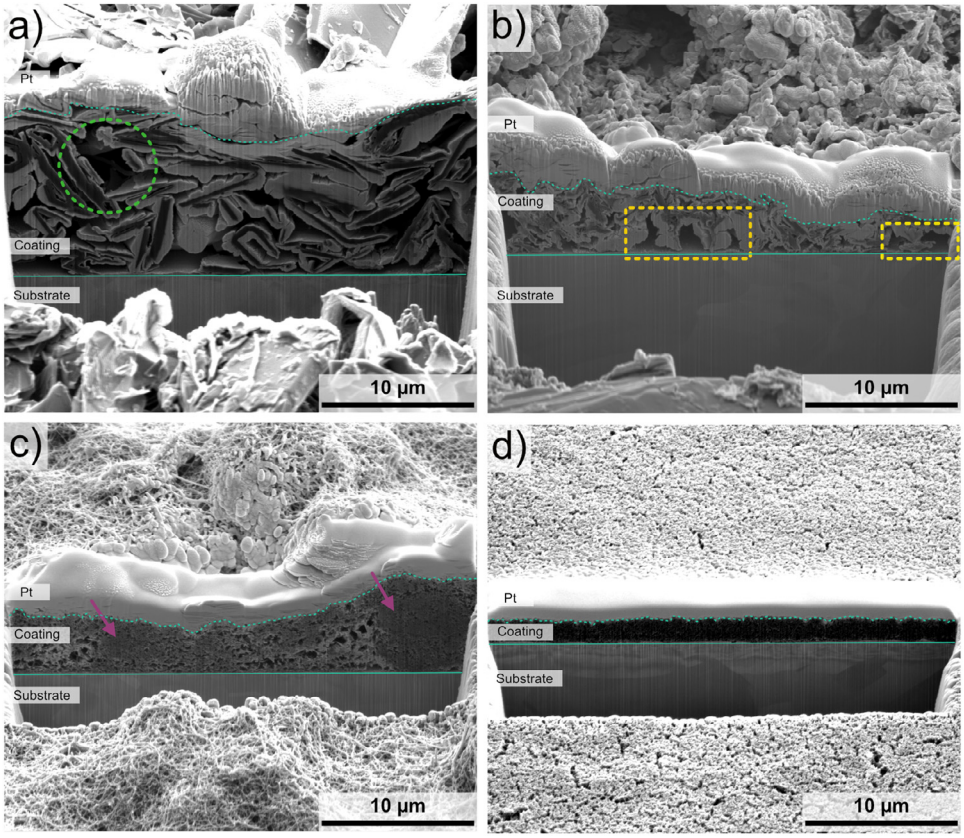

Fig. 4. FIB cross sections – a) GF, b) GO, c) CNT, and d) CNH. The green solid line indicates the substrate-coating interface. The green dashed line indicates the interface between the CNP coating and the protective Pt coating. The light green circle indicates a large void present in the GF coating. The violet arrows highlight compact regions in the CNT coating. The yellow squares highlight the porous interface between GO and the Cu substrate.

thick; however, this was expected since the particles are large in size. This cross section shows that the coating is not compact, with small voids (compared to the particle size). Larger voids are present in regions where the flakes were deposited in perpendicular direction relative to the previously deposited flake (highlighted in light green). The distance from the lowest point in the void, moving vertically towards the next GF, is approximately 4.1 µm. The maximum width of this void is approximately 5.8 µm. The different directions in which the flakes are deposited, as well as the presence of voids severely restricts the coating's ability to conduct electrical current. Therefore, the lack of compactness of this coating is undesirable for electrical applications. Nonetheless, this could be overcome by applying pressure during mating. Regarding atmospheric protection, the voids seen in the top-view micrograph do not appear as significant in the cross section. Although the superficial voids could allow atmospheric contaminants to penetrate. Nonetheless, the path towards the substrate is very intricate; no direct path is visible in this region of the coating. Concerning solid lubrication, the cross section shows some flakes that were deposited parallel to one another. This favors the solid-lubricating ability of graphite. Moreover, the interface between the graphite coating and the substrate raises concern. Only a few GF are in complete contact with the substrate, leaving large voids between the coating and the substrate. This is undesirable, as a weak bond between the coating and the substrate could facilitate the removal of the coating; thus, compromising the mechanical stability of the coating. However, this is beneficial for the lubricity of the system.

The GO coating is shown in **Fig. 4b**. Compared to the GF coating this coating seems more compact. Still large voids are present, especially near the coating-substrate interface. The GO coating is also thinner and more irregular, with an average thickness of 4.2 ± 1.2 µm. The standard deviation here represents a 27% variation in coating thickness in the region analyzed. This is a consequence of large GO agglomerates that significantly increase the thickness in some regions. This correlates with what was observed in SEM (**Fig. 2b**), since the topography of the coating appeared uneven throughout the coating. Many small voids are present within the core of the coating, with relatively larger voids near the substrate. As already stated, the presence of voids is highly unfavorable for electrical conduction, wear and atmospheric protection, and from a mechanical standpoint. The voids are non-conductive regions, which increase the overall electrical resistance of the coating. In addition, the presence of a porous network within the coating hinders the protection of the substrate from atmospheric conditions. This was inferred from the SEM micrographs, and now demonstrated by the ubiquitous presence of voids. Furthermore, the larger voids at the interface potentially reduce the coating's adhesion to the substrate (highlighted in yellow); consequently reducing the mechanical stability of the coating and facilitating its removal. These voids have a maximum width ranging from 1.0 to 3.2 µm. The left-most highlighted void has the largest vertical distance of approximately 3.3 µm.

The CNT coating's cross section is shown in **Fig. 4c**. This coating is comparatively more compact than the GF and GO coatings. A micro-porous network and some larger-sized voids can be seen. However, the voids are significantly smaller than in the previous two coatings. With the same deposition time, this coating results a bit thicker than the GO coating, but significantly thinner than the GF coating. It has an average thickness of 5.5 ± 1.5 µm. For the region analyzed, this coating also presents 27% variation in thickness. This was expected, since CNT tend to form large agglomerates, which were clearly visible in the SEM micrograph. The CNT coating presents dark regions where the coating appears very compact, with some identifiable small voids (shown by the violet ar-

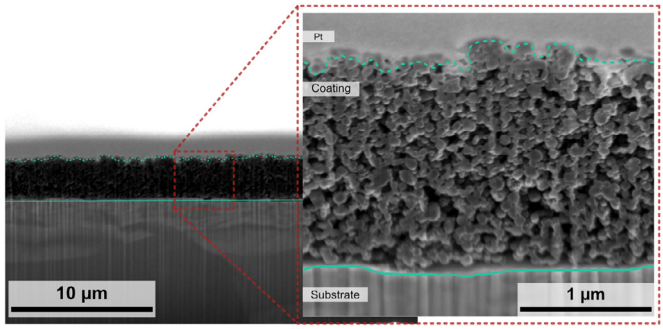

Fig. 5. Zoomed-in image showing the micro-porous network of the CNH coating. The green solid line highlights the substrate-coating interface, whereas the green dashed line highlights the interface between the CNH coating and the protective Pt coating.

rows). The small region highlighted (left arrow) has a maximum width of about 2.9 µm, whereas the larger region (right arrow) has a maximum width of 6.6 µm. These regions may be larger CNT agglomerates that were not broken apart during the dispersion process. Lighter regions represent areas with lower CNT density and larger voids. Nonetheless, this coating appears to be the most favorable for electrical current flow, atmospheric protection, and solid-state lubrication. Regarding the former, although many small voids are present, the CNT appear to have an adequate interconnection between the different regions of the coating. Consequently, this coating provides different pathways for electrons to be conducted from the electrode towards the substrate. Likewise, this is also an advantage for atmospheric protection since the lack of connection between voids blocks the flow of atmospheric contaminants towards the substrate. The larger voids observed in the lighter regions were measured. The average pore width is 0.55 µm. Although, they present a standard deviation of 0.25 µm, showing that within the larger voids there is significant variation in their dimensions. Moreover, this coating presents a seamless interface with the substrate. Some regions show voids at the interface; however, they are relatively small. Additionally, within the region with voids at the interface, CNT particles can be seen extending towards the substrate. This is of great interest since it promotes a better adhesion of the coating to the substrate.

Finally, the CNH coating's cross section is shown in **Fig. 4d**. As deduced from the SEM micrograph of the coating's surface (**Fig. 2d**), this coating is very thin, uniform, and compact. It has an average thickness of 1.8 µm with a standard deviation of 0.2 µm. The variation in thickness accounts for about 9% in the region analyzed, further proving the uniformity of the coating. The fissures that were observed on the coating's surface do not seem to extend within the coating (in the region analyzed), thus they do not affect the potential atmospheric protection of the coating. However, due to the thin nature of the coating, it is hard to visualize. Therefore, **Fig. 5** shows the coating at a larger magnification. In this image, the micro-porous network of the coating can be clearly observed. Observing this micrograph, many small voids can be identified. However, the CNH are connected to one another forming a complex structure of bonded particles, which in turn potentially enhances the coating's atmospheric protection behavior. Regarding the coating's electrical properties, the complex CNH network could hinder the electron transport properties. Nonetheless, there are multiple paths for the electrical current to flow towards the substrate due to the interconnected network of the CNH. Furthermore, as a consequence of the particle morphology, their potential as solid lubricants is of great interest. The voids present an average width of 0.12 µm with a standard deviation of 0.04 µm. From **Fig. 4d**, the CNH-substrate interface appears smooth and seamless.

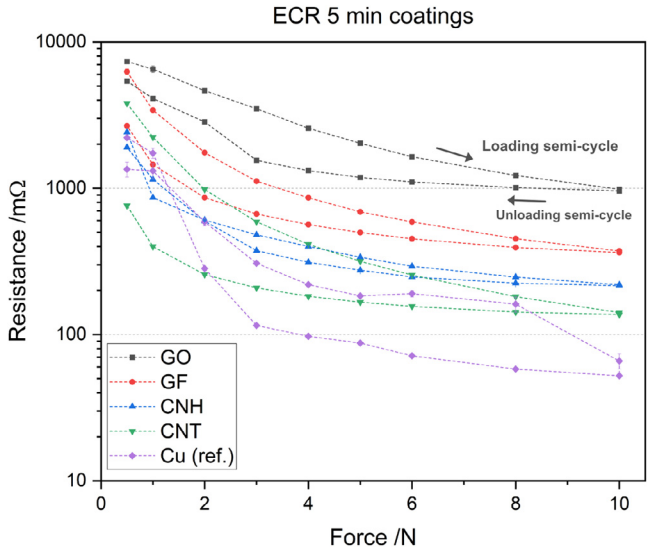

Fig. 6. Load-dependent ECR of coated and reference samples. The arrows indicate the direction in which the loading and unloading semi-cycles were carried out.

However, as **Fig. 5** shows, that is not the case. The voids found throughout the coating also extend to the interface, with few CNH particles in contact with the substrate. This has the potential to reduce the mechanical stability of the coating, allowing for an effortless removal of the coating after mating and un-mating cycles of a coated electrical contact.

All coatings were produced with a deposition time of five minutes. Considering the ratio between the mean particle/agglomerate size of the CNP (7.09, 5.01, 6.61, and 0.26 µm for GF, GO, CNT, and CNH, respectively) and the mean coating thickness (12.8, 4.24, 5.53, and 1.8 µm for GF, GO, CNT, and CNH, respectively), it can be stated that CNH has the highest deposition rate of all four nanoparticles. It is followed by GF; however, its deposition rate is significantly lower than CNH. GO and CNT have the lowest deposition rates. These nanoparticles have similar mean agglomerate sizes, and both produce coatings that are similar in thickness.

In addition to deposition time, voltage is also an important parameter. Since it is the electric field who imparts the electrophoretic force on the dispersed nanoparticles, which in turn is determined by the voltage applied; therefore, larger nanoparticles require larger voltages. Consequently, the small particle and cluster size of CNH (and by maintaining 300 V on all depositions) explains the higher deposition rate of CNH nanoparticles. This also justifies why GO and CNT have similar deposition rates, since these CNP have similar particle sizes. However, GF's deposition rate was not expected. Considering that GF are relatively large, it was anticipated that it would have the lowest deposition rate. Nonetheless, on account of the larger dimensions of the particles, thick coatings were expected.

3.4. Single-cycle electrical characterization

Load-dependent ECR values are shown in **Fig. 6**. The curves shown on the plot correspond to one measurement cycle (a loading semi-cycle and an unloading semi-cycle). The arrows indicate the loading and unloading directions. As a consequence of the values recorded, the nanovoltmeter was used with a range of 1 V to measure the four coatings, whereas 0.1 V was used for the copper reference sample (to minimize uncertainty in this measurements) [78]. All semi-cycles show the same tendency, i.e., higher ECR for lower loads, which is expected. This is a consequence of the compression of the coatings. As the normal load increases, the coat-

ings are compacted by the counter electrode, thus filling the voids within the coatings, and therefore improving the connectivity of the nanoparticles. Furthermore, as the load increases the round-headed counter electrode's apparent contact area also increases; consequently increasing the real contact area as well. In addition - due to the elastic behavior of the coatings - as the counter electrode compresses the coatings, it is immersed. This immersion of the rivet further increases the contact area. As the coatings are compacted - and the apparent contact area increases - so does the real contact area. The real contact area increases as the asperities (a-spots) of the electrodes come into electrical contacts. The elasticity of the coating increases the real contact area, approximating it to the apparent contact area. This is highly sought-after since it reduces the constriction resistance of the system by augmenting the a-spots that are in electrical contact.

As the figure shows, there is a clear hierarchy in the resistance of the coatings and substrate. As expected, the copper substrate has the lowest resistance at 10 N with a value of 52 mΩ. The substrate is followed by the CNT, CNH, GF, and GO coatings with 141 mΩ, 219 mΩ, 373 mΩ, and 985 mΩ at 10 N, respectively. This hierarchy was expected since GO and GF present high anisotropy in their transport properties. As the FIB cross sections shown in **Fig. 4a** and **Fig. 4b** these nanoparticles are randomly deposited, presenting different particle orientations. Ideally, the GF and GO particles should be deposited vertically. In that case these coatings would conduct the electrons in-plane, direction in which their electrical conductivity is higher. Nonetheless, within the randomly distributed coating, some particles were deposited in a more-or-less vertical direction, improving the electrical properties of the coating in these regions. However, this is more prominent in the GF coating. Since GF particles are larger, it is crucial that there is interconnectivity between the particles, considering that the voids generated within the coating are consequently also larger. Particularly for the GO coating, the oxygen atoms present in the structure due to the synthesis method hinder the nanoparticle's electrical properties. In addition to this particle's anisotropy, oxygen atoms act as scattering sites for the electrons; therefore, the electrical resistance increases. Moreover, the interface between the GO coating and the substrate affects its electrical properties. Among the four coatings analyzed, GO presents the weakest interface (shown by the porous interface in the FIB cross, **Fig. 4b**). Consequently, higher contact forces must be applied to achieve an adequate electrical contact between the counter electrode, coating, and substrate. The GF coating also presents a weak interface, however, not as significantly as GO. Voids present at the interface in the GO coating represent up to 70% of the coating's thickness. Whereas the dimension of the voids located at the interface in the GF coating are insignificant relative to the thickness of the coating (accounting for less than 15% of the coating thickness). Moreover, both coatings show elastic behavior since the ECR curves follow nearly the same tendency in the loading and unloading semi-cycle. It is interesting to point out that although the GF coating is more than twice as thick as the GO coating, the thickness does not play as a significant role as previously hypothesized. It was initially believed that thinner coatings would present lower ECR, however, these two coatings prove that the orientation of the nanoparticles is of greater importance than overall thickness (for these specific CNP).

The behavior of the CNH coating was unexpected, showing the second-best electrical behavior of the analyzed coatings. Due to the morphology of the particles (dahlia-shaped particle constituted of single-walled CNT with horn-shaped caps at their ends and semiconducting behavior) and it being a semiconducting CNP, it was not expected that it would show ECR values similar to that of the CNT coating. However, it was expected that the CNT coating would have lower resistance among the four CNP. Since multi-walled CNT were used, these nanoparticles always behave as metallic conductors. Nonetheless, for low contact forces in the loading semi-cycle, the CNT coating shows higher ECR values than CNH (3.8 Ω against 2.5 Ω). The CNH coating has a highly elastic behavior. Its ECR curve is very narrow, with the final value being similar to the initial value (1.9 Ω and 2.4 Ω, respectively). On the other hand, after the unloading semi-cycle the CNT coating presents significantly lower resistance than the CNH coating (0.76 Ω). These two coatings also present the advantage that they are relatively thin (especially the CNH coating). Thin coatings require lower normal loads for the counter electrode to reach the substrate, compacting the coating and reducing the film resistance. The compacting process allows for a better contacting area between the counter electrode, coating, and substrate, improving the real contact area and thus reducing the constriction resistance. Therefore, the resistance of the entire system is not significantly elevated. At maximum load (10 N), the resistance difference between the CNT and CNH coating is 80 mΩ (approximately 140 mΩ and 220 mΩ, respectively). Although these resistances seem low, they are extremely high compared to the values of the copper substrate. The substrate has an ECR of approximately 60 mΩ at 10 N. The CNT coating has more than double the resistance, whereas the CNH coating almost quadruple that resistance. However, these values are still relatively low considering that copper is one of the metals with the best electrical conductivity. This makes it is difficult to enhance copper's intrinsic electrical properties. Any additional layer added to this outstanding conductor significantly affects the conductivity of the pure metal. Nonetheless, at low normal loads the ECR values recorded for the copper substrate are comparable to the resistances of the coatings. This is because low normal loads do not puncture the native oxide layer that is formed on its surface. After puncturing this oxide layer however, the resistance of the substrate rapidly decreases. At 0.5 and 1 N the substrate shows the lowest resistance out of all the samples (approximately 1.5 Ω), when only considering the loading semi-cycle. However, the values do not differ significantly from the initial values of the CNH coating (about 2 Ω). At 2 N the resistance of the substrate is identical to that of the CNH coating. For the subsequent loads the resistance continues decreasing, reaching the lowest value at 10 N. As a consequence of the lower range used for the substrate's measurement (0.1 V), the measurements have a lower uncertainty. Therefore, at 10 N the value corresponding to the loading semi-cycle differs slightly from the value corresponding to the unloading semi-cycle. This difference detected may be caused by plastic flow of the substrate at this load. On the substrate, the ECR at low loads in the unloading semi-cycle is higher than the corresponding values during the loading semi-cycle. This is a consequence of the deficient contact between the copper sample and the counter electrode when unloading. As the load increases, the surface of the copper was deformed by the round counter electrode. During the unloading semi-cycle, as the load is gradually reduced, the real contact area decreases at a higher rate (fewer a-spots are in contact) due to the deformation that has occurred during the loading semi-cycle. With the normal load below 2 N the real contacting area is small, causing the ECR values to be comparable to the CNH coating. The same phenomenon was observed for the CNH coating, showing higher ECR at 0.5 N in the unloading semi-cycle than in the loading semi-cycle. This is a consequence of the thin nature of the coating. Due to the thickness of the GF, GO, and CNT coating, the resistance in the unloading semi-cycle is always lower than in the loading semi-cycle. Thus, enhancing the electrical contact between the coatings and the counter electrode even at low loads.

3.5. Post single-cycle ECR coating characterization

After carrying out the ECR measurements, the rivets and the coatings were observed under CLSM. The parameters of the CLSM

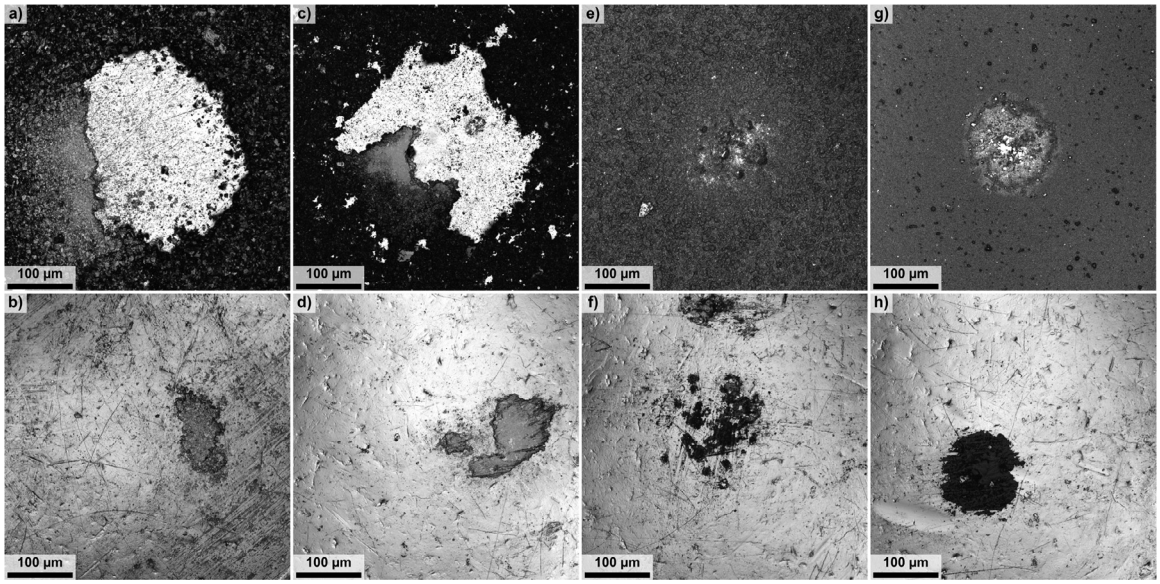

Fig. 7. CLSM intensity profile of CNP coating (top) and Au rivet (bottom); a-b) GF, c-d) GO, e-f) CNT, and g-h) CNH after one ECR measurement cycle.

are identical to those described in *Section 2*. Before observing the rivets under CLSM they were wiped with paper cloth and later cleaned with compressed air. The images are shown in **Fig. 7a-h**. The GF coating and the rivet's surfaces after ECR are shown **Fig. 7a** and **Fig. 7b**, respectively. The GF coating was partially removed after the electrical measurements. Part of the removed coating was deposited on the rivet itself. Graphite was also found remaining on the paper used to wipe the rivet before observing under the microscope. Although, the coating was not entirely removed. The mark left behind by the indenting counter electrode was circumscribed; the resulting circle had a diameter of approximately 470 µm. Similarly, the coating that was deposited on the rivet after the measurements was circumscribed resulting in a diameter of approximately 235 µm. The GO coating and rivet after ECR are shown in **Fig. 7c** and **Fig. 7d**, respectively. This coating was also partially removed after the ECR measurements, in similar manner as the GF coating. Moreover, the counter electrode was also partially coated. The diameter of the circumscribed mark left behind by the indenting counter electrode is approximately 460 µm. Regarding the coated rivet, it has a diameter of approximately 275 µm. GO particles were cleaned away when wiping the rivet before observing under CLSM. Observing the CNT coating and rivet, **Fig. 7e** and **Fig. 7f** respectively, it can be seen that the mark left correlates perfectly to the deposition on the rivet. The mark and deposition have an approximate diameter of 250 µm. The coating's surface shows that part of the CNT were removed, but to a lesser extent compared to the previous coatings. In the mark we can also see darker regions, which correspond to CNT agglomerates that remain in the indented area. Likewise, the image of the rivet shows areas with high concentration of CNT and areas without CNT. These images coincide, i.e., the intensity map of the coating shows CNT agglomerates in regions where the rivet does not show CNT particles. Likewise, the rivet shows regions with CNT deposited where the coating shows partial removal of the coating. No traces of CNT particles were observed when wiping the rivet after the measurement cycle. Finally, the CNH coating and rivet are shown in **Fig. 7g** and **Fig. 7h**. The intensity map of the coating shows partial removal of the nanoparticles on the outer 'ring' of the indented area, showing little to no CNH particles in the center of the circumference. The diameter of the interaction zone is approximately 220 µm, whereas the deposited CNH particles in the rivet has a diameter of approximately 200 µm. A clear correlation between the indented region in the coating and the CNH deposition in the rivet can be observed. As for CNT, no traces of CNH particles were observed after wiping the rivet.

The different interaction zones of the indenting counter electrode are interesting. They provide information on the compression that the coatings have undergone, but also on the mechanical stability of the coatings. Observing the intensity maps of the GF and GO coatings - **Fig. 7a** and **Fig. 7c**, respectively - it is evident that the coating was removed at a higher rate than in the case of CNT and CNH, **Fig. 7e** and **Fig. 7g**. As described in *Section 3.2*, the GF and GO coatings have a very weak interface with the substrate. The interface presents multiple large voids which hinder the adhesion of the coating to the substrate. Consequently, the coating is easily removed by the indenting counter electrode. Comparing the areas where the GF and GO coatings were removed with the areas on the rivet where the respective CNP were deposited, the latter is in the range of half of the former (470 µm to 235 µm and 460 µm to 275 µm, respectively). This shows that the coating area removed is higher than that deposited on the rivet. Additionally, these two coatings left behind CNP residue on the rivet, which was wiped away after the ECR measurements. This further demonstrates the fragility of these two coatings due to lack of adhesion with the substrate. The higher amount of CNP removed can be attributed to weaker adhesion to the substrate, compared to the adhesion between CNP. Consequently, when retracting the counter electrode, the CNP deposited on the counter electrode remove the CNP in the vicinity of the contact area. The CNT and CNH coatings, on the other hand, show a similar behavior regarding the diameter of the circumscribed area affected in the coating and deposited nanoparticle on the rivet's surface (250 µm in both cases for CNT and 220 µm to 200 µm for CNH). As the FIB cross sections from *Section 3.2* demonstrated, these two coatings present a better interface. That is, the coating-substrate interfaces are seamless (especially compared to the GF and GO). Therefore, the mechanical stability of the coating is superior. This is the reason why the area affected in the coatings matches the area affected in the rivets. The interaction between the CNP and the substrate is stable enough to prevent additional CNP removal when retracting the counter electrode.

3.6. Dual-cycle electrical characterization

Multiple loading and unloading semi-cycles provide useful information on the elasticity of the proposed coatings. An advantage

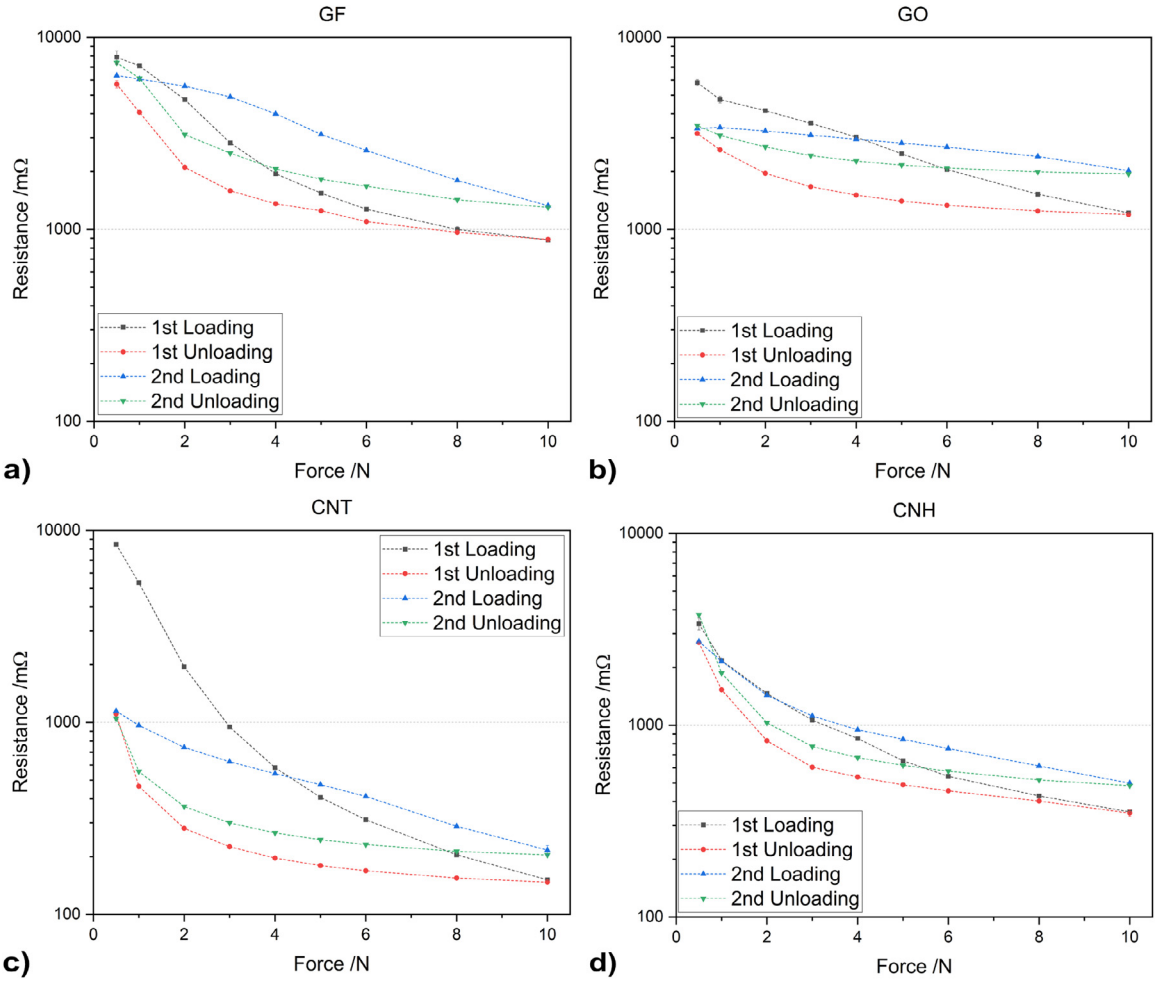

Fig. 8. Load-dependent ECR of coated samples over two cycles of a) GF, b) GO, c) CNT, and d) CNH. The gray line depicts the ECR values on the first loading semi-cycle, whereas the red line shows the first unloading semi-cycle. The blue and green line depict the ECR values of the second loading and unloading semi-cycles, respectively.

of CNP coatings is the ability of the coatings to return, to a certain degree, to their original form after the load has been removed. This elastic restitution of the coatings ensures repeatability in the contacting area after the first mating and un-mating cycle. Furthermore, this behavior improves the contacting area, consequently reducing the constriction resistance. Two-cycle ECR measurements were carried out on the four coatings produced. The ECR curves are shown in **Fig. 8**. As the figure shows, the coatings behave similarly on both measurement cycles. The most elastic coating measured was the CNH coating, since the curve corresponding to the first cycle is nearly the same for the second cycle. The least elastic coating measured was the CNT coating, showing high ECR values initially (for low loads in the first loading cycle). However, as the measurement cycle progresses, the resistance decreases and remains relatively low. The GF and GO behave in a similar manner. These coatings are not as elastic as the CNH coating, but these also do not show a significant decrease after the first loading cycle like the CNT coating. Between GF and GO, GO shows slightly more elasticity than GF. This is due to the inherent high flexibility and mechanical strength of the graphene nanoparticles. Furthermore, as observed in *Section 3.2*, GO particles form large networks. When loading on these GO clusters they will deform, copying the curved shape of the counter electrode. Contrarily, GF particles do not form clusters or agglomerates. In addition, GF particles are randomly oriented when deposited. Graphite interlayers interact weakly with one another. Therefore, when loading on a GF particle - displacing the particle from its original position - there is no restitution force. Consequently, the elasticity of the coating is relatively low.

The elasticity of the CNH coating can be attributed to two key factors, i.e., the compactness of the coating and intrinsic properties of the nanoparticle. The latter refers to the fact that CNH particles, when compressing a nanohorn axially, are capable of absorbing energy. When the compressing force is removed, the energy absorbed returns the nanohorn to its original shape. This property fundamentally guarantees an elastic coating. Although the CNH coating presents a porous network, the voids are small in dimensions. Therefore, when applying a normal load on the coating, the force does not significantly compact the coating; thus, the coating behaves elastically since the displacement is marginal.

Although the CNT coating does not show an elastic behavior in the first loading semi-cycle, in the subsequent semi-cycles it behaves moderately elastic. Nonetheless, this coating shows the lowest ECR values. All measurements taken after the first loading semi-cycle above 1 N normal load show an ECR value below 1000 mΩ. The minimum resistance value for this coating was observed at 10 N in the first unloading semi-cycle, with a resistance of approximately 150 mΩ. However, this coating also shows the highest initial ECR value in the first loading semi-cycle at 0.5 N, with an approximate value of 8460 mΩ. The initial high values of ECR may be a consequence of the large CNT agglomerates. Due to the geometry of CNT, when compressed radially, the electrostatic forces restitute the original shape of the CNT when the load is re-

Table 3
. Summary of key findings.

	GF	GO	CNT	CNH
Topography	Very low homogeneity	Low homogeneity	Mild homogeneity	High homogeneity
Compactness	High porosity	Moderately high porosity	Mild porosity	High compactness
Mean thickness /μm	12.8 ± 0.9	4.2 ± 1.2	5.5 ± 1.5	1.8 ± 0.2
Coating-substrate interface	Weak	Weak	Moderate	Seamless
Deposition rate	Moderate	Low	Low	Very high
ECR at 10 N /mΩ	373	985	141	219
Elastic restitution	Moderate	Moderate	(Initially) Low	Very high

moved. However, CNT agglomerates are formed by weakly-bonded CNT. Thus, the first loading semi-cycle breaks apart the CNT agglomerates, producing smaller agglomerates. Therefore, in the subsequent semi-cycles the resistance of the system is different from the first semi-cycle since the contacting surfaces are not the same.

In all cases, for high normal loads, the resistance of the system in the first cycle is higher than in the second cycle. This is a consequence of the deformation of the substrate. In the first loading semi-cycle, the substrate is mirror polished. As the load increases, the counter electrode penetrates the CNP coatings reaching the substrate. Consequently, the hard gold rivet indents the surface of the substrate deforming it. On the second cycle the counter electrode contacts the deformed surface. This should decrease the constriction resistance, approximating the real contact area to the apparent contact area. However, if that were the case, the resistance should decrease instead. The increase in electrical resistance in the second cycle (compared to the first unloading semi-cycle) may be a consequence of a deficient contact between the electrodes. For the analyzed coatings, the resistance values at 10 N in the first cycle is between 60% and 70% of the ECR values - at the same load - in the second cycle. Furthermore, the unloading semi-cycles show the lowest average resistance values throughout the entire semi-cycles. This behavior is a consequence of the coating. When unloading, the contact area between the counter electrode and the sample is gradually decreases. However, as the load on the coatings decreases, the CNP gradually return - approximately - to their initial positions, mimicking the geometry of the counter electrode. Therefore, as the load decreases the decrease in contact area is compensated by the coating, improving the electrical contact between the counter electrode and the coated sample.

The following table (**Table 3**) summarizes the key findings of this work. Through this study, it was determined that CNH coatings produce the most homogeneous topographies, followed by CNT, then GO, and GF the most heterogeneous topographies. Regarding compactness, CNH produce highly compact coatings, followed by CNT, then GO, with GF producing the most porous coatings. CNT and CNH coatings present adequate adhesion compared to GO and GF coatings, which show weak interactions with the substrate. The highest deposition rate was observed for CNH. GF follows, although with a much lower deposition rate. GO and CNT show similar deposition rates, the lowest out of the CNP in question. CNT present the lowest ECR at 10 N, followed by CNH and GF. GO shows the highest ECR at 10 N, with values close to 1000 mΩ. GF and GO coatings behave moderately elastic in multi-cycle ECR measurements. CNT showed the least elastic behavior, however after the first semi-cycle the elasticity moderately increased. CNH showed the highest elasticity out of the four CNP.

4. Conclusions

Four different CNP were deposited on copper substrates via EPD. Load-dependent ECR measurements showed that, for normal loads above 4 N, the resistance of the systems was always below 1 Ω, except for coatings produced with GO. The oxygen atoms present in GO act as scatter sites for the electros, hindering this coatings conductivity. Additionally, oxygen generates lattice defects in the graphene structure which further compromise the conductivity. CNT and CNH coatings proved the most favorable coatings. At 10 N the CNT and CNH coatings showed the lowest and second lowest ECR, respectively. Furthermore, although the CNT coating did not show an elastic behavior for the first loading semi-cycle, it did behave elastically for subsequent semi-cycles. On the other hand, the CNH coating shows a clear elastic behavior throughout both measurement cycles. Additionally, these coatings' interfaces with the substrate are seamless, thus guaranteeing a better adhesion and mechanical stability. Finally, these two coatings produce thin and uniform - in the case of CNH - coatings. Accordingly, these two CNP coatings have the potential application of protecting and lubricating electrical connectors for the following reasons:

- Both CNT and CNH have been proven effective as solid-state lubricants.
- They produce relatively compact coatings and have a hydrophobic behavior for atmospheric protection by manipulating their surface chemistry.
- Both CNT and CNH have high thermal conduction coefficients, thus dissipating the heat produced by Joule's effect.
- Above 4 N normal load, CNT and CNH showed ECR values below 400 mΩ.

In future works, it is of interest to analyze the ideal coating thicknesses (i.e., EPD duration) for the different CNP based on the ECR values measured. Moreover, tribological testing on the coatings produces is of interest. Fretting and scratch tests would help quantify the lubricating behavior of the CNP coatings and their adhesion, respectively. Additionally, different copper alloys are of interest, thus obtaining a wider understanding on how the substrate influences the deposition rate, adhesion, and electrical behavior of the systems. Furthermore, substituting GO with rGO can be a promising alternative for electrical contact applications. The absence of oxygen and fewer lattice defects in the graphene structure should improve the ECR of the coating. In addition, sessile drop tests are of interest; therefore analyzing the wetting behavior of the different CNP coatings.

Declaration of Competing Interest

The authors declare that they have no known competing financial interests or personal relationships that could have appeared to influence the work reported in this paper.

Acknowledgements

B. Alderete wishes to acknowledge the support from the German Academic Exchange Service (DAAD). The authors gratefully acknowledge funding in the ZuMat project, supported by the State of Saarland from the European Regional Development Fund (Europäischen Fonds für Regionale Entwicklung, EFRE).

References

[1] P. van Dijk, Critical aspects of electrical connector contacts, in: Proc. 21st Int. Conf. Electr. Contacts, Zurich, 2002.
[2] P.G. Slade (Ed.), Electrical Contacts Pinrciples and Applications, Second Edi, Taylor & Francis, Boca Raton, 2014.
[3] E.H.L. Falcao, F. Wudl, Carbon allotropes: beyond graphite and diamond, J. Chem. Technol. Biotechnol 82 (2007) 524–531, doi:10.1002/jctb.1693.
[4] A. Hirsch, The era of carbon allotropes, Nat. Mater. 9 (2010) 868–871, doi:10.1038/nmat2885.
[5] B. Zhmud, B. Pasalskiy, Nanomaterials in lubricants: An industrial perspective on current research, Lubricants 1 (2013) 95–101, doi:10.3390/lubricants1040095.
[6] Y. Chen, P. Renner, H. Liang, Dispersion of nanoparticles in lubricating oil: a critical review, Lubricants 7 (2019), doi:10.3390/lubricants7010007.
[7] W. Dai, B. Kheireddin, H. Gao, H. Liang, Roles of nanoparticles in oil lubrication, Tribol. Int. 102 (2016) 88–98, doi:10.1016/j.triboint.2016.05.020.
[8] W. Bollman, J. Spreadborough, Action of Graphite as a Lubricant, Nature 186 (1960) 29–30, doi:10.1038/186029a0.
[9] H. Wang, Graphite solid lubrication materials, in: Q.J. Wang, Z.-W. Chung (Eds.), Encycl. Tribol., Springer US, Boston, MA, 2013, pp. 1550–1555, doi:10.1007/978-0-387-92897-5_1261.
[10] T.W. Scharf, S.V. Prasad, Solid lubricants: A review, J. Mater. Sci. 48 (2013) 511–531, doi:10.1007/s10853-012-7038-2.
[11] H.E. Sliney, Solid Lubrificants, 1991. https://ntrs.nasa.gov/api/citations/19910013083/downloads/19910013083.pdf.
[12] F.J. Clauss, Solid Lubricants and Self-Lubricating Solids, Academic Press, New York and London, 1972.
[13] E.R. Braithwaite, Solid Lubricants and Surfaces, Pergamon Press Ltd.g, Oxford, 1964.
[14] C.-G. Lee, Y.-J. Hwang, Y.-M. Choi, J.-K. Lee, C. Choi, J.-M. Oh, A study on the tribological characteristics of graphite nano lubricants, Int. J. Precis. Eng. Manuf. 10 (2009) 85–90, doi:10.1007/s12541-009-0013-4.
[15] Z.J. Zhang, D. Simionesie, C. Schaschke, Graphite and hybrid nanomaterials as lubricant additives, Lubricants 2 (2014) 44–65, doi:10.3390/lubricants2020044.
[16] G. Fugallo, A. Cepellotti, L. Paulatto, M. Lazzeri, N. Marzari, F. Mauri, Thermal conductivity of graphene and graphite: Collective excitations and mean free paths, Nano Lett 14 (2014) 6109–6114, doi:10.1021/nl502059f.
[17] E. Planes, L. Flandin, N. Alberola, Polymer composites bipolar plates for PEMFCs, Energy Procedia 20 (2012) 311–323, doi:10.1016/j.egypro.2012.03.031.
[18] W. Park, J. Hu, L.A. Jauregui, X. Ruan, Y.P. Chen, Electrical and thermal conductivities of reduced graphene oxide/polystyrene composites, Appl. Phys. Lett. 104 (2014), doi:10.1063/1.4869026.
[19] A. Kozbial, F. Zhou, Z. Li, H. Liu, L. Li, Are Graphitic Surfaces Hydrophobic? Acc. Chem. Res. 49 (2016) 2765–2773, doi:10.1021/acs.accounts.6b00447.
[20] K.S. Novoselov, V.I. Fal'Ko, L. Colombo, P.R. Gellert, M.G. Schwab, K. Kim, A roadmap for graphene, Nature 490 (2012) 192–200, doi:10.1038/nature11458.
[21] C.N.R. Rao, K. Biswas, K.S. Subrahmanyam, A. Govindaraj, Graphene, the new nanocarbon, J. Mater. Chem. 19 (2009) 2457–2469, doi:10.1039/b815239j.
[22] A.K. Geim, Graphene : Status and Prospects, Science 324 (80) (2009) 1530–1535, doi:10.1126/science.1158877.
[23] D.G. Papageorgiou, I.A. Kinloch, R.J. Young, Mechanical properties of graphene and graphene-based nanocomposites, Prog. Mater. Sci. 90 (2017) 75–127, doi:10.1016/j.pmatsci.2017.07.004.
[24] I.N. Kholmanov, C.W. Magnuson, A.E. Aliev, H. Li, B. Zhang, J.W. Suk, L.L. Zhang, E. Peng, S.H. Mousavi, A.B. Khanikaev, R. Piner, G. Shvets, R.S. Ruoff, Improved electrical conductivity of graphene films integrated with metal nanowires, Nano Lett 12 (2012) 5679–5683, doi:10.1021/nl302870x.
[25] D. Berman, A. Erdemir, A.V. Sumant, Graphene: A new emerging lubricant, Mater. Today. 17 (2014) 31–42, doi:10.1016/j.mattod.2013.12.003.
[26] L. Liu, M. Zhou, L. Jin, L. Li, Y. Mo, G. Su, X. Li, H. Zhu, Y. Tian, Recent advances in friction and lubrication of graphene and other 2D materials: Mechanisms and applications, Friction 7 (2019) 199–216, doi:10.1007/s40544-019-0268-4.
[27] R.K. Singh, R. Kumar, D.P. Singh, Graphene oxide: Strategies for synthesis, reduction and frontier applications, RSC Adv 6 (2016) 64993–65011, doi:10.1039/c6ra07626b.
[28] Y. Zhu, S. Murali, W. Cai, X. Li, J.W. Suk, J.R. Potts, R.S. Ruoff, Graphene and graphene oxide: Synthesis, properties, and applications, Adv. Mater. 22 (2010) 3906–3924, doi:10.1002/adma.201001068.
[29] M.S.A. Bhuyan, M.N. Uddin, M.M. Islam, F.A. Bipasha, S.S. Hossain, Synthesis of graphene, Int. Nano Lett. 6 (2016) 65–83, doi:10.1007/s40089-015-0176-1.
[30] C. Botas, P. Álvarez, P. Blanco, M. Granda, C. Blanco, R. Santamaría, L.J. Romasanta, R. Verdejo, M.A. López-Manchado, R. Menéndez, Graphene materials with different structures prepared from the same graphite by the Hummers and Brodie methods, Carbon N. Y. 65 (2013) 156–164, doi:10.1016/j.carbon.2013.08.009.
[31] N.I. Zaaba, K.L. Foo, U. Hashim, S.J. Tan, W.W. Liu, C.H. Voon, Synthesis of Graphene Oxide using Modified Hummers Method: Solvent Influence, Procedia Eng 184 (2017) 469–477, doi:10.1016/j.proeng.2017.04.118.
[32] V.B. Mohan, R. Brown, K. Jayaraman, D. Bhattacharyya, Characterisation of reduced graphene oxide: Effects of reduction variables on electrical conductivity, Mater. Sci. Eng. B Solid-State Mater. Adv. Technol. 193 (2015) 49–60, doi:10.1016/j.mseb.2014.11.002.
[33] H. Liang, Y. Bu, J. Zhang, Z. Cao, A. Liang, Graphene oxide film as solid lubricant, ACS Appl. Mater. Interfaces. 5 (2013) 6369–6375, doi:10.1021/am401495y.
[34] A. Senatore, V. D'Agostino, V. Petrone, P. Ciambelli, M. Sarno, Graphene oxide nanosheets as effective friction modifier for oil lubricant: materials, methods, and tribological results, ISRN Tribol. 2013 (2013) 1–9, doi:10.5402/2013/425809.
[35] P. Wu, X. Chen, C. Zhang, J. Zhang, J. Luo, J. Zhang, Modified graphene as novel lubricating additive with high dispersion stability in oil, Friction 9 (2021) 143–154, doi:10.1007/s40544-019-0359-2.
[36] G. Wang, B. Wang, J. Park, J. Yang, X. Shen, J. Yao, Synthesis of enhanced hydrophilic and hydrophobic graphene oxide nanosheets by a solvothermal method, Carbon N. Y. 47 (2009) 68–72, doi:10.1016/j.carbon.2008.09.002.
[37] L. Xu, J. Teng, L. Li, H.D. Huang, J.Z. Xu, Y. Li, P.G. Ren, G.J. Zhong, Z.M. Li, Hydrophobic graphene oxide as a promising barrier of water vapor for regenerated cellulose nanocomposite films, ACS Omega 4 (2019) 509–517, doi:10.1021/acsomega.8b02866.
[38] R. Saito, G. Dresselhaus, M.S. Dresselhaus, Physical Properties of Carbon Nanotubes, Imperial College Press, London, 1998, doi:10.1142/p080.
[39] M.S. Dresselhaus, G. Dresselhaus, R. Saito, Physics of carbon nanotubes, Carbon N. Y. 33 (1995) 883–891, doi:10.1016/0008-6223(95)00017-8.
[40] V.N. Popov, Carbon nanotubes: properties and application, Mater. Sci. Eng. R Reports. 43 (2004) 61–102, doi:10.1016/j.mser.2003.10.001.
[41] T.W. Ebbesen, Carbon nanotubes, Chem. Eng. News. 79 (2001) 11.
[42] S. Nasir, M.Z. Hussein, Z. Zainal, N.A. Yusof, Carbon-based nanomaterials/allotropes: a glimpse of their synthesis, properties and some applications, Materials (Basel) 11 (2018) 1–24, doi:10.3390/ma11020295.
[43] N. Saifuddin, A.Z. Raziah, A.R. Junizah, Carbon nanotubes: A review on structure and their interaction with proteins, J. Chem. 2013 18 (2013), doi:10.1155/2013/676815.
[44] M. Moniruzzaman, K.I. Winey, Polymer nanocomposites containing carbon nanotubes, Macromolecules 39 (2006) 5194–5205, doi:10.1021/ma060733p.
[45] C. Li, E.T. Thostenson, T.W. Chou, Sensors and actuators based on carbon nanotubes and their composites: a review, Compos. Sci. Technol 68 (2008) 1227–1249, doi:10.1016/j.compscitech.2008.01.006.
[46] P. Kim, L. Shi, A. Majumdar, P.L. McEuen, Thermal transport measurements of individual multiwalled nanotubes, Phys. Rev. Lett. 87 (2001) 215502-1-215502-4, doi:10.1103/PhysRevLett.87.215502.
[47] J. Klinovaja, M.J. Schmidt, B. Braunecker, D. Loss, Carbon nanotubes in electric and magnetic fields, Phys. Rev. B - Condens. Matter Mater. Phys 84 (2011), doi:10.1103/PhysRevB.84.085452.
[48] E.M. Pérez, N. Martín, π-π Interactions in carbon nanostructures, Chem. Soc. Rev. 44 (2015) 6425–6433, doi:10.1039/c5cs00578g.
[49] B. Alderete, T. MacLucas, D. Espin, S.P. Brühl, F. Mücklich, S. Suarez, Near superhydrophobic carbon nanotube coatings obtained via electrophoretic deposition on low-alloy steels, Adv. Eng. Mater. (2021), doi:10.1002/adem.202001448.
[50] L. Reinert, F. Lasserre, C. Gachot, P. Grützmacher, T. MacLucas, N. Souza, F. Mücklich, S. Suarez, Long-lasting solid lubrication by CNT-coated patterned surfaces, Sci. Rep. 7 (2017) 1–13, doi:10.1038/srep42873.
[51] L. Reinert, S. Suarez, A. Rosenkranz, Tribo-mechanisms of carbon nanotubes: friction and wear behavior of CNT-reinforced nickel matrix composites and CNT-coated bulk nickel, Lubricants 4 (2016) 11, doi:10.3390/lubricants4020011.
[52] L. Reinert, I. Green, S. Gimmler, B. Lechthaler, F. Mücklich, S. Suàrez, Tribological behavior of self-lubricating carbon nanoparticle reinforced metal matrix composites, Wear 408-409 (2018) 72–85, doi:10.1016/j.wear.2018.05.003.
[53] J.A.C. Cornelio, P.A. Cuervo, L.M. Hoyos-Palacio, J. Lara-Romero, A. Toro, Tribological properties of carbon nanotubes as lubricant additive in oil and water for a wheel-rail system, J. Mater. Res. Technol. 5 (2016) 68–76, doi:10.1016/j.jmrt.2015.10.006.
[54] F. Dassenoy, L. Joly-Pottuz, J.M. Martin, T. Mieno, in: V.N. Popov, P. Lambin (Eds.), Carbon Nanotubes as Advanced Lubricant Additives, Carbon Nanotub, Springer Netherlands, 2006, pp. 237–238.
[55] J. Kaluzny, A. Merkisz-Guranowska, M. Giersig, K. Kempa, Lubricating performance of carbon nanotubes in internal combustion engines - engine test results for CNT enriched oil, Int. J. Automot. Technol 18 (2017) 1047–1059 https://doi.org/10.1007/s12239−017−0102−9.
[56] N. Karousis, I. Suarez-Martinez, C.P. Ewels, N. Tagmatarchis, Structure, properties, functionalization, and applications of carbon nanohorns, Chem. Rev. 116 (2016) 4850–4883, doi:10.1021/acs.chemrev.5b00611.
[57] S. Zhu, G. Xu, Single-walled carbon nanohorns and their applications, Nanoscale 2 (2010) 2538–2549, doi:10.1039/c0nr00387e.
[58] T. MacLucas, S. Suarez, On the solid lubricity of electrophoretically deposited carbon nanohorn coatings, Lubricants 7 (2019), doi:10.3390/lubricants7080062.
[59] M. Yudasaka, S. Iijima, V.H. Crespi, Single-wall carbon nanohorns and nanocones, Top. Appl. Phys. 111 (2008) 605–629, doi:10.1007/978-3-540-72865-8_19.
[60] D. Maharaj, B. Bhushan, S. Iijima, Effect of carbon nanohorns on nanofriction and wear reduction in dry and liquid environments, J. Colloid Interface Sci. 400 (2013) 147–160, doi:10.1016/j.jcis.2013.03.008.
[61] Y. Tao, D. Noguchi, C.M. Yang, H. Kanoh, H. Tanaka, M. Yudasaka, S. Iijima, K. Kaneko, Conductive and mesoporous single-wall carbon nanohorn/organic aerogel composites, Langmuir 23 (2007) 9155–9157, doi:10.1021/la701660w.
[62] P. Karfa, S. De, K.C. Majhi, R. Madhuri, P.K. Sharma, Functionalization of carbon nanostructures, in: D.L. Andrews, R.H. Lipson, T. Nann (Eds.), Compr. Nanosci. Nanotechonlogy, Second, Academic Press, 2019, pp. 123–144, doi:10.1016/B978-0-12-803581-8.11225-1.
[63] A.R. Boccaccini, J. Cho, J.A. Roether, B.J.C. Thomas, E.Jane Minay, M.S.P. Shaffer, Electrophoretic deposition of carbon nanotubes, Carbon N. Y. 44 (2006) 3149–3160, doi:10.1016/j.carbon.2006.06.021.

[64] J.H. Dickerson, A.R. Boccaccini, Electrophoretic Deposition of Nanomaterials, 2nd Ed., 2011, doi:10.1007/978-1-4614-4605-7.
[65] P. Sarkar, P.S. Nicholson, Electrophoretic deposition (EPD): mechanisms, kinetics, and application to ceramics, J. Am. Ceram. Soc. 79 (1996) 1987–2002, doi:10.1111/j.1151-2916.1996.tb08929.x.
[66] H.C. Hamaker, Formation of a Deposit by Electrophoresis, Trans. Faraday Soc 30 (1940) 279–287.
[67] M. Farrokhi-Rad, T. Shahrabi, Electrophoretic deposition of titania nanoparticles: sticking parameter determination by an in situ study of the EPD kinetics, J. Am. Ceram. Soc. 95 (2012) 3434–3440, doi:10.1111/j.1551-2916.2012.05402.x.
[68] M. Atiq Ur Rehman, Q. Chen, A. Braem, M.S.P. Shaffer, A.R. Boccaccini, Electrophoretic deposition of carbon nanotubes: recent progress and remaining challenges, Int. Mater. Rev. 0 (2020) 1–30, doi:10.1080/09506608.2020.1831299.
[69] Y. Ma, J. Han, M. Wang, X. Chen, S. Jia, Electrophoretic deposition of graphene-based materials: a review of materials and their applications, J. Mater. 4 (2018) 108–120, doi:10.1016/j.jmat.2018.02.004.
[70] L. Reinert, M. Zeiger, S. Suarez, V. Presser, F. Mücklich, Dispersion analysis of carbon nanotubes, carbon onions, and nanodiamonds for their application as reinforcement phase in nickel metal matrix composites, RSC Adv 5 (2015) 95149–95159, doi:10.1039/c5ra14310a.
[71] M.F. De Riccardis, D. Carbone, A. Rizzo, A novel method for preparing and characterizing alcoholic EPD suspensions, J. Colloid Interface Sci. 307 (2007) 109–115, doi:10.1016/j.jcis.2006.10.037.
[72] A. Loyd, J. Hemond, R. Martens, A preliminary investigation of graphite, graphene and carbon nanotubes (CNT's) as solid state lubricants, Electr. Contacts, in: Proc. Annu. Holm Conf. Electr. Contacts, 2011, pp. 22–30, doi:10.1109/HOLM.2011.6034776.
[73] R. Puyol, S. Suarez, A contact resistance measurement setup for the study of novel contacts, IEEE URUCON (2017) 1–4, doi:10.1109/URUCON.2017.8171881.
[74] K.E. Trinh, E. Ramos-Moore, I. Green, C. Pauly, M. Zamanzade, F. Mucklich, Topographical and microstructural effects of laser surface texturing on tin-coated copper electrical connectors under load cycling, IEEE Trans. Components, Packag. Manuf. Technol 7 (2017) 582–590, doi:10.1109/TCPMT.2017.2659224.
[75] K.E. Trinh, F. Mücklich, E. Ramos-Moore, The role of microstructure and surface topography in the electrical behavior of Sn-coated Cu contacts, in: 27th Int. Conf. Electr. Contacts, ICEC 2014 - Proc., 2014, pp. 243–248.
[76] TektronixLow Level Measurements Handbook, Precision DC Current, 7th Editio, Voltage and Resistance Measurements, Beaverton, 2016 https://download.tek.com/document/LowLevelHandbook_7Ed.pdf.
[77] E.M. Bock, Low-level contact resistance characterization, AMP J. Technol. 3 (1993) 64–68.
[78] B. Alderete, R. Puyol, S. Slawik, E. Espin, F. Mücklich, S. Suarez, Multipurpose setup used to characterize tribo-electrical properties of electrical contact materials, MethodsX 8 (2021) 101498, doi:10.1016/j.mex.2021.101498.